Quantum Precision Limits of Displacement Noise-Free Interferometers

Tuvia Gefen,[1] Rajashik Tarafder[2,3] Rana X. Adhikari,[3] and Yanbei Chen[2]

[1]*Institute for Quantum Information and Matter, California Institute of Technology, Pasadena, California 91125, USA*
[2]*Theoretical Astrophysics, Walter Burke Institute for Theoretical Physics,*
California Institute of Technology, Pasadena, California 91125, USA
[3]*LIGO Laboratory, California Institute of Technology, Pasadena, California 91125, USA*

Current laser-interferometric gravitational wave detectors suffer from a fundamental limit to their precision due to the displacement noise of optical elements contributed by various sources. Several schemes for displacement noise-free interferometers (DFI) have been proposed to mitigate their effects. The idea behind these schemes is similar to decoherence-free subspaces in quantum sensing; i.e., certain modes contain information about the gravitational waves but are insensitive to the mirror motion (displacement noise). We derive quantum precision limits for general DFI schemes, including optimal measurement basis and optimal squeezing schemes. We introduce a triangular cavity DFI scheme and apply our general bounds to it. Precision analysis of this scheme with different noise models shows that the DFI property leads to interesting sensitivity profiles and improved precision due to noise mitigation and larger gain from squeezing.

Introduction.—Quantum metrology studies fundamental precision limits in physical measurements imposed by quantum physics. Recent progress in this field has led to formulation of precision limits for a variety of sensing devices: gravitational wave (GW) detectors [1–8], magnetometers [9,10], atomic clocks [11–14], nano-NMR [15–19], etc.

We focus here on optomechanical sensors and laser interferometers. These platforms have emerged as the primary instruments for the detection of GWs, with successful observations conducted by several of these detectors [20–24]. They are, however, severely limited by noise sources that displace the mirror positions in the interferometer: thermal noise, radiation pressure noise (RPN), seismic noise, and Newtonian gravity noise [25–29]. These noises are, in particular, dominant in the low-frequency regime (< 10 Hz), thus limiting the sensitivity at this range and preventing detection of various signals such as intermediate-mass black holes, young neutron stars, extreme mass ratio inspirals, etc. Circumventing displacement noise is thus an outstanding challenge for GW detection and optomechanical sensors in general.

Interestingly, the coupling of light fields to GW signals is different from their coupling to mirror displacement; i.e., GW information is accumulated along the optical path, unlike displacement noise which is only introduced at the mirrors. This observation has led to proposals of interferometers wherein displacement noise can be canceled while not losing the GW signal [30]. This approach is referred to as displacement noise-free interferometry (DFI).

DFI for laser interferometry was originally proposed using a simplified system and later expanded to more complex systems such as speed meters and 3D interferometers [31–36]. A similar approach for laser phase noise cancellation has also been proposed for LISA using time delay interferometry [37–39]. However, DFI systems with requisite sensitivities remain elusive. Furthermore, a rigorous study of the quantum precision limits of these interferometers has not been conducted.

In this Letter, we use quantum metrology techniques to derive general precision limits, optimal measurements, and optimal squeezing quadratures for DFI schemes. We develop a triangular cavity DFI scheme, which combines resonance power amplification and DFI, and apply our results to analyze it. In addition to the improved sensitivity at low frequencies, we observe interesting effects that motivate the use of DFI and multichannel interferometers. We identify pseudo-displacement-free subspaces, i.e., subspaces that are displacement-free for a limited range of frequencies. These subspaces lead to unexpected sensitivity profiles and further noise suppression. Lastly, we study the effect of squeezing and show that DFI increases the sensitivity gain from squeezing in the high displacement noise regime.

Formalism and model.—Previous DFI schemes used several Mach-Zender interferometers [31,32]. However, these interferometers did not incorporate cavity resonance to amplify the power and sensitivity. Here, we propose a scheme that combines DFI with cavity resonance gain: an equilateral triangular cavity with three mirrors, six input local-oscillator fields, and six outputs. The six fields circulate inside the cavity—split between the clockwise and anticlockwise directions. The scheme and suggested
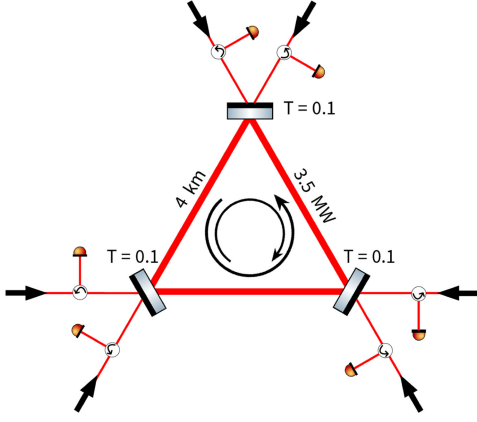
FIG. 1. Sketch of the DFI scheme. A symmetric triangular cavity is formed by three mirrors and six input laser fields. Six detectors are placed in the opposite direction of the input fields. The configuration leads to both a clockwise and an anticlockwise circulating field within the cavity. We used the following parameters. Arm length, $L = 4$ km; laser wavelength, 1064 nm (same as advanced LIGO [40]). Mirror's mass, 5 kg; intracavity power, 3.5 MW (to enhance RPN for illustrations). Power transmissivity of the mirrors, $T = 0.1$.

parameters are described in Fig. 1. This triangular cavity yields power amplification: given identical mirrors transmissivities (T), the ratio between the intracavity power and the total input power is $T/[3(1 - \sqrt{1-T})^2]$.

We will show that this scheme is indeed a DFI. The intuition for this is simple: the displacement noise is generated by the three mirrors and induced on the six output fields. Since the number of mirrors is smaller than the number of output fields, we have modes that are decoupled from this noise and enable the DFI. This approach is formulated below.

We use a general formulation that holds for any system with n mirrors and k fields, such that $k > n$. The system is described using the input-output formalism [41,42], and we denote the quadrature operators of the input and output fields as

$$\hat{\mathbf{Q}}_{\text{in}} = \begin{pmatrix} \hat{\mathbf{a}}_1 \\ \hat{\mathbf{a}}_2 \end{pmatrix}, \quad \hat{\mathbf{Q}}_{\text{out}} = \begin{pmatrix} \hat{\mathbf{b}}_1 \\ \hat{\mathbf{b}}_2 \end{pmatrix},$$

respectively. $\hat{\mathbf{a}}_1$, $\hat{\mathbf{b}}_1$ are the k-dimensional vectors of amplitude quadratures, and $\hat{\mathbf{a}}_2$, $\hat{\mathbf{b}}_2$ are the k-dimensional vectors of phase quadratures. These quadratures satisfy standard commutation relations: $[(\hat{\mathbf{Q}}_{\text{out}})_l, (\hat{\mathbf{Q}}_{\text{out}})_k] = J_{l,k}$ with

$$J = i \begin{pmatrix} 0 & \mathbb{1}_k \\ -\mathbb{1}_k & 0 \end{pmatrix}$$

(same for $\hat{\mathbf{Q}}_{\text{in}}$). The noisy displacement of the mirrors is denoted as $\{\Delta x_i\}_{i=1}^n$, and the amplitude of the GW

polarization vector is given by $\mathbf{h} = (h_+, h_\times)^T$. The input-output relations in the frequency domain are then

$$\hat{\mathbf{Q}}_{\text{out}}(\Omega) = M(\Omega)\hat{\mathbf{Q}}_{\text{in}}(\Omega) + \mathcal{V}(\Omega)\mathbf{h}(\Omega) + A(\Omega)\mathbf{\Delta x}(\Omega). \quad (1)$$

$\Omega = 2\pi f$ is the angular frequency, hereafter this notation will be suppressed, M, A, $\mathcal{V}$ are the transfer matrices of the input modes, displacement noise, and the GW vector, respectively. Accordingly, these are $(2k \times 2k)$-, $(2k \times n)$-, and $(2k \times 2)$-dimensional matrices, that take the following general form (assuming carrier frequency is resonant with the arm length):

$$M = \begin{pmatrix} M_{\text{int}} & 0 \\ M_{21} & M_{\text{int}} \end{pmatrix}, \quad A = \begin{pmatrix} 0 \\ A_{\text{ph}} \end{pmatrix},$$

$$\mathcal{V} = \begin{pmatrix} 0 \\ \mathcal{V}_{\text{ph}} \end{pmatrix} = \begin{pmatrix} 0 & 0 \\ \mathcal{V}_{+,\text{ph}} & \mathcal{V}_{\times,\text{ph}} \end{pmatrix}. \quad (2)$$

M_{int} is a $k \times k$ unitary interferometer transfer matrix and M_{21} is a $k \times k$ coupling matrix between the amplitude and phase quadratures due to radiation pressure noise. A, $\mathcal{V}$ act only on the phase quadratures, with their support being A_{ph} [$(k \times n)$ dimensional], $\mathcal{V}_{\text{ph}}$ [$(k \times 2)$ dimensional]. $\mathcal{V}_{\text{ph}}$ consists of two column vectors: $\mathcal{V}_{+,\text{ph}}, \mathcal{V}_{\times,\text{ph}}$; these are k-dimensional transfer vectors of $h_+, h_\times$, respectively. A detailed description of how to calculate these transfer matrices can be found in Refs. [42,43].

We are now poised to define the displacement free subspace (DFS): this is the space of phase quadratures of the form $\mathbf{u} \cdot \hat{\mathbf{b}}_2$, with $\mathbf{u} \in \ker(A_{\text{ph}}^\dagger)$. Since $\mathbf{u}^\dagger A_{\text{ph}}\mathbf{\Delta x} = 0$, these quadratures are decoupled from the displacement noise term in Eq. (1) and thus resilient to this noise. Thinking of the phase quadratures as k-dimensional column vectors, the DFS is then the kernel of $A_{\text{ph}}^\dagger$. We denote this subspace and its projection operator as M_{DFS} and Π_{DFS}, respectively. The orthogonal complement of the DFS is the coupled subspace; it is the linear span of the column vectors of A_{ph}. This subspace and its projection operator are denoted as M_C and Π_C, respectively. Since $A_{\text{ph}}^\dagger$ is an $(n \times k)$-dimensional matrix, a sufficient condition for the existence of DFS is $k > n$, i.e., more fields than mirrors.

Quantum precision limits.—Our figure of merit is the minimal detectable GW amplitude in any given polarization. With our interferometer, the dominant polarization is approximately h_+, hence the figure of merit is the standard deviation in estimating h_+; we denote it as σ and refer to it as the standard deviation (SD) or the sensitivity. This reduces the problem to a single parameter estimation of h_+, where the sensitivity is calculated below using the Cramér-Rao bound.

According to the Cramér-Rao bound, given a readout scheme with outcomes distribution $\{p(x)\}_x$, the variance σ^2 of any unbiased estimator of h_+ satisfy $\sigma^2 \geq F^{-1}$, with

$F = \langle [\partial_{h_+} \ln(p)]^2 \rangle$ being the Fisher information (FI). This lower bound is asymptotically light [44].

In the quantum context, further optimization over the detection schemes yields the quantum Fisher information (QFI), denoted as I [45], such that for any readout scheme $\sigma^2 \geq I^{-1}$.

In our case the QFI has a particularly simple form [8,46,47],

$$I = 2(\partial_{h_+} \mathbf{d}_q)^\dagger \Sigma_q^{-1} (\partial_{h_+} \mathbf{d}_q), \qquad (3)$$

where $\mathbf{d_q}$ and Σ_q are the mean vector and covariance matrix of $\hat{\mathbf{Q}}_{\text{out}}$, respectively:

$$\mathbf{d_q} = \langle \hat{\mathbf{Q}}_{\text{out}} \rangle, \quad (\Sigma_q)_{i,j} = \langle \{\hat{\mathbf{Q}}_{\text{out},i}, \hat{\mathbf{Q}}_{\text{out},j}^\dagger\} \rangle - \langle \hat{\mathbf{Q}}_{\text{out},i} \rangle \langle \hat{\mathbf{Q}}_{\text{out},j}^\dagger \rangle. \qquad (4)$$

with $\{\bullet, \bullet\}$ being the anti-commutator of the operators. This simple form is because the output modes are in Gaussian state, and information about $\mathbf{h}$ is encoded only in the $\mathbf{d_q}$.

From Eqs. (1) and (2) we observe that $\partial_{h_+} \mathbf{d}_q = \mathcal{V}_+$, with $\mathcal{V}_+ = (0 \; \mathcal{V}_{+,\text{ph}})^T$, and that $\Sigma_q = M\Sigma_i M^\dagger + A\Sigma_{\Delta\mathbf{x}} A^\dagger$, where Σ_i, $\Sigma_{\Delta\mathbf{x}}$ are the covariance matrices of the input quadratures and the displacement noise $\Delta\mathbf{x}$, respectively. Assuming the input state is vacuum and the displacement noise is Gaussian i.i.d., $\Delta\mathbf{x} \sim N(0, \frac{1}{2}\delta^2 \mathbb{1})$, the covariance matrix is then $\Sigma_q = \frac{1}{2}(MM^\dagger + \delta^2 AA^\dagger)$, and the QFI reads:

$$I = 4\mathcal{V}_+^\dagger (MM^\dagger + \delta^2 AA^\dagger)^{-1} \mathcal{V}_+. \qquad (5)$$

In Eq. (5), the RPN is included in the $MM^\dagger$ term, and the rest of the displacement noise is encoded by the additional $AA^\dagger$ term. The shot noise limit is obtained by nullifying the RPN and the displacement noise, i.e., M is unitary and $\delta = 0$, which yields $I = 4\mathcal{V}_+^\dagger \mathcal{V}_+$. This limit serves as an upper bound to any noisy QFI scenario.

The QFI [Eqs. (3) and (5)] is attainable with a homodyne measurement of the quadrature $(\Sigma_q^{-1} \mathcal{V}_+) \cdot \hat{\mathbf{Q}}_{\text{out}}$ [43,48]. Our sensitivity curves will therefore correspond to either the QFI, i.e., the SD with an optimal measurement, $\sigma = 1/\sqrt{I}$, or to the FI with a specific homodyne measurement, $\sigma = 1/\sqrt{F}$.

Precision limits of the simplified model.—We begin with a simplified model to develop an understanding of the DFI method. The simplified model is devoid of RPN, i.e., M is unitary, and the displacement noise is taken to be a white noise, i.e., $\delta(\Omega)$ is constant. The QFI is, therefore,

$$I = 4\mathcal{V}_+^\dagger (\mathbb{1} + \delta^2 AA^\dagger)^{-1} \mathcal{V}_+. \qquad (6)$$

The sensitivity for different levels of δ, ranging from the shot noise limit ($\delta = 0$) to infinite displacement noise ($\delta \to \infty$), is presented in Fig. 2(a). The DFI property is manifested in the fact that as $\delta \to \infty$, the standard deviation remains finite, denoted by the black line in Fig. 2(a). We thus have finite noise in GW detection even in the presence of infinite displacement noise.
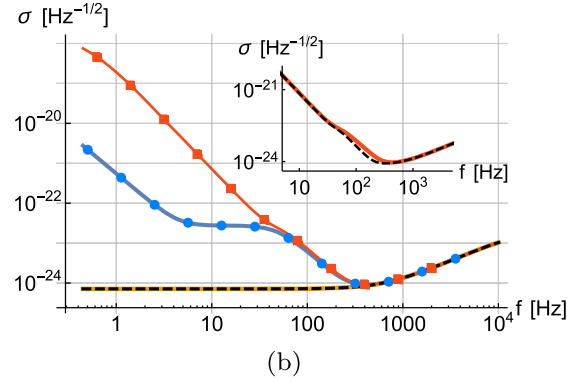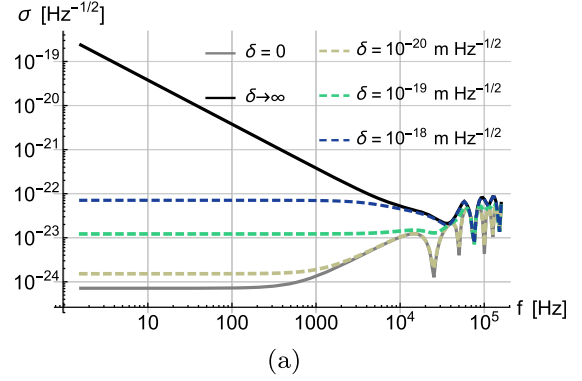

(a)

(b)

FIG. 2. (a) Precision limits with the simplified model. The SD, σ, as a function of frequency for different levels of displacement noise (δ) [Eq. (6)]. The DFI property is manifested in the fact that σ is finite in the limit of infinite displacement noise (solid black curve). (b) Precision limits with realistic noise profiles. Given RPN alone, by measuring the optimal quadratures [Eq. (8)] the QFI (black dashed line) coincides with the shot noise limit (solid yellow line). On the other hand, measuring the (nonoptimal) phase quadratures yields the solid blue (circles) line [Eq. (9)]. Similarly, given both RPN and thermal noise, measuring the phase quadratures yields the solid red (rectangles) line. Inset: comparison between the phase quadratures FI (solid red line) and the QFI (black dashed line) in the presence of thermal noise and RPN.

To understand the behavior of the sensitivity, we note that the QFI can be decomposed as

$$I = F_C + F_{\text{DFS}}$$
$$= 4\mathcal{V}_+^\dagger \Pi_C (\mathbb{1} + \delta^2 AA^\dagger)^{-1} \Pi_C \mathcal{V}_+ + 4\mathcal{V}_+^\dagger \Pi_{\text{DFS}} \mathcal{V}_+. \qquad (7)$$

The first term (F_C) is the information from the coupled subspace and the second term (F_{DFS}) is the information from the DFS.

In the infinite displacement noise limit ($\delta \to \infty$), the first term F_C vanishes and thus the QFI in this limit is

$$I_{\delta \to \infty} = 4\mathcal{V}_+^\dagger \Pi_{\text{DFS}} \mathcal{V}_+;$$

i.e., we get information only from the DFS. As $f \to 0$, this standard deviation diverges, indicating that in this regime

$\Pi_{\text{DFS}}\mathcal{V}_+ \to 0$. For finite δ [dashed lines in Fig. 2(a)], the QFI converges to $I \approx (4/\delta^2)\mathcal{V}_+^\dagger(AA^\dagger)^{-1}\mathcal{V}_+$ at low frequencies, and thus σ grows as δ in this limit.

Furthermore, using Eq. (7) we can quantify the effectiveness of the DFI with the following coefficient: $\eta = [F_{\text{DFS}}/(F_{\text{DFS}} + F_C)]$, i.e., the fraction of the information that comes from the DFS. It will be shown that η has an operational meaning as the gain from squeezing in the limit of large displacement noise.

Precision limits with realistic noise profiles.—Let us now consider the sensitivity with realistic thermal noise and RPN. We begin by analyzing the effect of RPN alone and then study the combination of the two noises.

The effect of RPN is given by a nonunitary M, i.e., nonzero M_{21} matrix [Eq. (2)]. We assume that the mirrors are free masses; hence, $M_{21} \propto (1/m\Omega^2)$, where m is the mass of the mirrors. This typically leads to a sensitivity profile that scales as Ω^{-2} [7,8].

The QFI, in this case, saturates the shot noise limit [black dashed line in Fig. 2(b)]; i.e., RPN is completely removed by measuring an appropriate choice of quadratures. This is a generalization of the optimal frequency-dependent readout introduced in Refs. [2,49]. Specifically, the k quadratures given by the column vectors of the matrix

$$T_{\text{dec}} = \begin{pmatrix} -M_{\text{int}}M_{21}^\dagger \\ \mathbb{1} \end{pmatrix} \qquad (8)$$

are decoupled from RPN, and homodyne measurement of the corresponding k operators, $T_{\text{dec}}^\dagger\hat{\mathbf{Q}}_{\text{out}}$, saturates the QFI and the shot noise limit.

Measuring these optimal quadratures is experimentally challenging; the standard and simple readout quadratures are the phase quadratures. Phase quadratures, however, are not decoupled from RPN and measuring them yields the following FI [43]:

$$F = 4\mathcal{V}_{+,\text{ph}}^\dagger(\mathbb{1} + M_{21}M_{21}^\dagger)^{-1}\mathcal{V}_{+,\text{ph}}. \qquad (9)$$

This expression is analogous to the QFI of the simplified model [Eq. (6)], where the term $M_{21}M_{21}^\dagger$ is the displacement noise caused by RPN. It can be shown that $M_{21} = A_{\text{ph}}D_x$, where D_x is the transfer matrix of the amplitude quadratures to the displacement of the mirrors [43]. The DFS is therefore decoupled from this noise. The corresponding sensitivity is presented in the solid blue line (circles) of Fig. 2(b), where we observe an interesting behavior: unlike the conventional sensitivity curves, it does not diverge uniformly as $1/\Omega^2$ [50], instead there is a range of frequencies where the divergence stops. This plateau is due to a pseudo-DFS, a subspace that is impervious to displacement noise in this range of frequencies. Let us further elaborate on this.

In our triangular cavity scheme the phase quadratures can be decomposed to three orthogonal eigenspaces of the covariance matrix: $M_{\min} \oplus M_{\max} \oplus M_{\text{DFS}}$, where $M_{\min} \oplus M_{\max}$ is a decomposition of M_C to eigenspaces with minimal and maximal eigenvalues, respectively. Since these are eigenspaces of the covariance matrix, the FI is a sum of the FIs achieved with each one of them separately; i.e., $F = F_{\min} + F_{\max} + F_{\text{DFS}}$. For different frequencies, different subspaces are dominant; this accounts for the nonuniform divergence. The plateau appears when $F_{\min}$ becomes dominant. $M_{\min}$ is immune to displacement noise in this range of frequencies, i.e., it is an eigenspace of $M_{21}M_{21}^\dagger$ with an eigenvalue that is much smaller than shot noise, hence the plateau. This is discussed further in the Supplemental Material [43].

Let us now consider thermal noise as well. The thermal noise is modeled as $\Delta\mathbf{x} \sim N(0, \frac{1}{2}\delta^2\mathbb{1})$, where $\delta^2(f) = 2.7 \times 10^{-30}(1/f)^5 \text{m}^2/\text{Hz}$ [51]. Hence, the effect of thermal displacement noise is similar to the simplified model with a frequency-dependent δ.

In the presence of both RPN and thermal displacement noise, the optimal measurement quadratures are the quadratures of Eq. (8), which are decoupled from RPN. Hence RPN is completely canceled and we are left only with the thermal noise. The QFI thus takes the form of Eq. (6) with a frequency-dependent δ. A plot of the corresponding sensitivity is presented in the inset of Fig. 2(b).

Measuring the phase quadratures, RPN is not canceled and the FI reads $4\mathcal{V}_{+,\text{ph}}^\dagger(\mathbb{1} + M_{21}M_{21}^\dagger + \delta^2 A_{\text{ph}}A_{\text{ph}}^\dagger)^{-1}\mathcal{V}_{+,\text{ph}}$. The plot of the corresponding sensitivity profile (red solid line) and a comparison with the QFI (black dashed line) is presented in the inset of Fig. 2(b). Three different regimes can be observed in the plot, that correspond to three eigenspaces of the covariance matrix. For low enough frequencies, the DFS becomes dominant and the SD diverges as f^{-2}, instead of $f^{-5/2}$. Before that, there is an intermediate regime where $M_{\min}$ is dominant and a short plateau exists. The comparison in Fig. 2(b) (inset) between the phase quadratures FI and the QFI shows that they coincide at low frequencies where the thermal noise is dominant, but the QFI outperforms the phase quadratures FI at intermediate frequencies where RPN is dominant.

Effect of squeezing.—We summarize the optimal schemes and sensitivities with squeezing. Given a squeezing factor of e^{-r} the optimal QFI is $4\mathcal{V}_{+,\text{ph}}^\dagger(e^{-2r}\mathbb{1} + \delta^2 A_{\text{ph}}A_{\text{ph}}^\dagger)^{-1}\mathcal{V}_{+,\text{ph}}$; it can be achieved with squeezing of the phase quadratures and measuring the optimal quadratures of Eq. (8). For phase quadratures measurement, the optimal FI is $4\mathcal{V}_{+,\text{ph}}^\dagger[e^{-2r}(\mathbb{1} + M_{21}M_{21}^\dagger) + \delta^2 A_{\text{ph}}A_{\text{ph}}^\dagger]^{-1}\mathcal{V}_{+,\text{ph}}$, achievable by squeezing the optimal quadratures. These optimal squeezing quadratures and sensitivity bounds are derived in the Supplemental Material [43].

The performance of the squeezed schemes, and comparison with the unsqueezed case, is shown in Fig. 3. Observe that the gain from squeezing is not uniform and depends on the effectiveness of the DFI, i.e., on η. We can
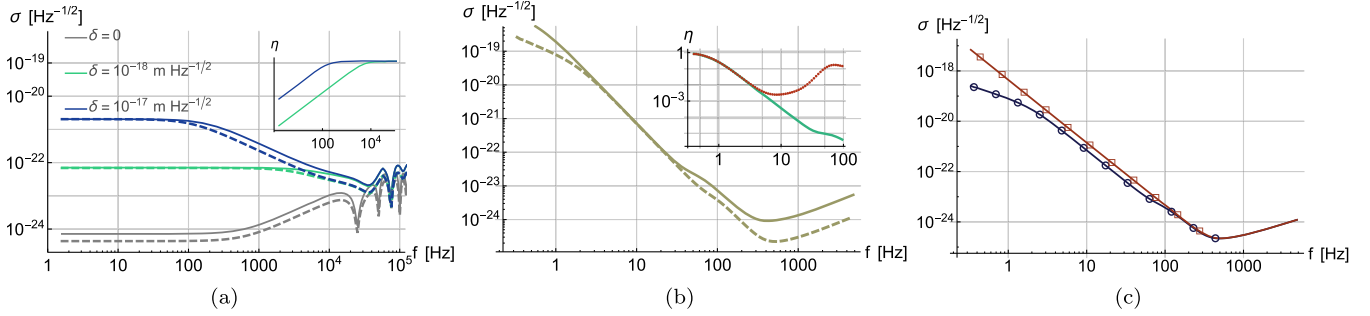
FIG. 3. Effect of squeezing. (a) Performance with squeezing in the simplified model. Dashed lines correspond to SD (σ) with squeezing and solid lines to unsqueezed. For white displacement noise, squeezing becomes not effective at lower frequencies as can be also observed from the plot of η in the inset. (b) Performance with squeezing given thermal noise and RPN. The solid (dashed) line corresponds to unsqueezed (optimally squeezed) SD with phase quadratures measurement. Inset: η_{gain} (red dots) and η (green line) as a function of frequency. (c) The SD with optimal squeezed input and optimal measurement (blue curve, circles) compared to the SD with the same squeezed input but a readout combination that maximizes the signal (red curve, squares).

define the gain from squeezing as $\eta_{\text{gain}} = [(F_{\text{sq}}/F - 1)/(e^{2r} - 1)]$, where $F_{\text{sq}}(F)$ is the FI with(out) squeezing. Clearly $0 \leq \eta_{\text{gain}} \leq 1$, where 0 corresponds to no gain and 1 to maximal gain. We show in the Supplemental Material [43] that in the limit of large displacement noise $\eta_{\text{gain}} = \eta$; hence η_{gain} equals the fraction of information coming from the DFS. This is illustrated in the insets of Figs. 3(a) and 3(b). DFI is therefore necessary to gain from squeezing in the presence of large displacement noise. The improvement introduced by DFI is summarized in Fig. 3(c) where we compare the sensitivity with squeezed input given different readout combinations: a combination that maximizes the signal and the optimal combination that saturates QFI. The sensitivity with optimal combination considerably outperforms the sensitivity with maximal-signal combination at low frequencies due to two DFI properties: better scaling with f (f^{-2} compared to $f^{-2.5}$), and larger gain from squeezing.

Extensions and conclusions.—The Supplemental Material contains extensions of this triangular scheme to n-gons with n mirrors [43]. Such polygon schemes may lead to further sensitivity improvement. The Supplemental Material also contains an analysis of the Sagnac noise, i.e., a phase shift due to rotation. We show that the resulting sensitivity loss is small.

To conclude, we developed new DFI schemes and derived general quantum precision limits, optimal measurements, and optimal squeezing quadratures.

There are still several challenges and open questions. The main challenge is to incorporate suppression of laser noise in this architecture. The laser noise must be correlated between the different ports, and the challenge is to engineer such correlation. Other challenges include further optimization over the architecture and considering also detuning.

[1] Carlton M. Caves, Quantum-mechanical noise in an interferometer, Phys. Rev. D **23**, 1693 (1981).

[2] H. J. Kimble, Yuri Levin, Andrey B. Matsko, Kip S. Thorne, and Sergey P. Vyatchanin, Conversion of conventional gravitational-wave interferometers into quantum nondemolition interferometers by modifying their input and/or output optics, Phys. Rev. D **65**, 022002 (2001).

[3] Judith Abadie, Benjamin P. Abbott, T. D. Abbott, M. R. Abernathy, Matthew Benacquista, Teviet Creighton, H. Daveloza, Maria E. Diaz, R. Grosso, Soumya Mohanty *et al.*, A gravitational wave observatory operating beyond the quantum shot-noise limit, Nat. Phys. **7**, 962 (2011).

[4] Mankei Tsang, Howard M. Wiseman, and Carlton M. Caves, Fundamental quantum limit to waveform estimation, Phys. Rev. Lett. **106**, 090401 (2011).

[5] Rafał Demkowicz-Dobrzański, Konrad Banaszek, and Roman Schnabel, Fundamental quantum interferometry bound for the squeezed-light-enhanced gravitational wave detector GEO 600, Phys. Rev. A **88**, 041802(R) (2013).

[6] Matthias D. Lang and Carlton M. Caves, Optimal quantum-enhanced interferometry using a laser power source, Phys. Rev. Lett. **111**, 173601 (2013).

[7] Haixing Miao, Rana X Adhikari, Yiqiu Ma, Belinda Pang, and Yanbei Chen, Towards the fundamental quantum limit of linear measurements of classical signals, Phys. Rev. Lett. **119**, 050801 (2017).

[8] Dominic Branford, Haixing Miao, and Animesh Datta, Fundamental quantum limits of multicarrier optomechanical sensors, Phys. Rev. Lett. **121**, 110505 (2018).

[9] Jonatan Bohr Brask, Rafael Chaves, and Jan Kołodyński, Improved quantum magnetometry beyond the standard quantum limit, Phys. Rev. X **5**, 031010 (2015).

[10] Tillmann Baumgratz and Animesh Datta, Quantum enhanced estimation of a multidimensional field, Phys. Rev. Lett. **116**, 030801 (2016).

[11] Katarzyna Macieszczak, Martin Fraas, and Rafał Demkowicz-Dobrzański, Bayesian quantum frequency estimation in presence of collective dephasing, New J. Phys. **16**, 113002 (2014).

[12] Hidetoshi Katori, Optical lattice clocks and quantum metrology, Nat. Photonics **5**, 203 (2011).

[13] Krzysztof Chabuda, Ian D. Leroux, and Rafał Demkowicz-Dobrzański, The quantum allan variance, New J. Phys. **18**, 083035 (2016).

[14] Raphael Kaubruegger, Denis V. Vasilyev, Marius Schulte, Klemens Hammerer, and Peter Zoller, Quantum variational optimization of Ramsey interferometry and atomic clocks, Phys. Rev. X **11**, 041045 (2021).

[15] Simon Schmitt, Tuvia Gefen, Felix M Stürner, Thomas Unden, Gerhard Wolff, Christoph Müller, Jochen Scheuer, Boris Naydenov, Matthew Markham, Sebastien Pezzagna et al., Submillihertz magnetic spectroscopy performed with a nanoscale quantum sensor, Science **356**, 832 (2017).

[16] Jens M. Boss, K. S. Cujia, Jonathan Zopes, and Christian L. Degen, Quantum sensing with arbitrary frequency resolution, Science **356**, 837 (2017).

[17] Nati Aharon, Amit Rotem, Liam P. McGuinness, Fedor Jelezko, Alex Retzker, and Zohar Ringel, NV center based nano-NMR enhanced by deep learning, Sci. Rep. **9**, 17802 (2019).

[18] D. Cohen, T. Gefen, L. Ortiz, and A. Retzker, Achieving the ultimate precision limit with a weakly interacting quantum probe, npj Quantum Inf. **6**, 83 (2020).

[19] Simon Schmitt, Tuvia Gefen, Daniel Louzon, Christian Osterkamp, Nicolas Staudenmaier, Johannes Lang, Matthew Markham, Alex Retzker, Liam P. McGuinness, and Fedor Jelezko, Optimal frequency measurements with quantum probes, npj Quantum Inf. **7**, 55 (2021).

[20] Benjamin P. Abbott, Richard Abbott, T. De Abbott, M. R. Abernathy, Fausto Acernese, Kendall Ackley, Carl Adams, Thomas Adams, Paolo Addesso, R. X. Adhikari et al., Observation of gravitational waves from a binary black hole merger, Phys. Rev. Lett. **116**, 061102 (2016).

[21] Benjamin P. Abbott, Rich Abbott, T. Dea Abbott, Fausto Acernese, Kendall Ackley, Carl Adams, Thomas Adams, Paolo Addesso, R. X. Adhikari, Vaishali B. Adya et al., Gw170817: Observation of gravitational waves from a binary neutron star inspiral, Phys. Rev. Lett. **119**, 161101 (2017).

[22] B. P. Abbott, Richard Abbott, T. Dea Abbott, S. Abraham, F. Acernese, K. Ackley, C. Adams, R. X. Adhikari, V. B. Adya, Christoph Affeldt et al., GWTC-1: A gravitational-wave transient catalog of compact binary mergers observed by LIGO and Virgo during the first and second observing runs, Phys. Rev. X **9**, 031040 (2019).

[23] R. Abbott, T. D. Abbott, S. Abraham, F. Acernese, K. Ackley, A. Adams, C. Adams, R. X. Adhikari, V. B. Adya, Christoph Affeldt et al., GWTC-2: Compact binary coalescences observed by LIGO and Virgo during the first half of the third observing run, Phys. Rev. X **11**, 021053 (2021).

[24] R. Abbott, T. D. Abbott, F. Acernese, K. Ackley, C. Adams, N. Adhikari, R. X. Adhikari, V. B. Adya, C. Affeldt, D. Agarwal et al., GWTC-3: Compact binary coalescences observed by LIGO and Virgo during the second part of the third observing run, Phys. Rev. X **13**, 041039 (2023).

[25] Peter R. Saulson, Terrestrial gravitational noise on a gravitational wave antenna, Phys. Rev. D **30**, 732 (1984).

[26] Scott A. Hughes and Kip S. Thorne, Seismic gravity-gradient noise in interferometric gravitational-wave detectors, Phys. Rev. D **58**, 122002 (1998).

[27] Jennifer C. Driggers, Jan Harms, and Rana X. Adhikari, Subtraction of Newtonian noise using optimized sensor arrays, Phys. Rev. D **86**, 102001 (2012).

[28] Jan Harms, Terrestrial gravity fluctuations, Living Rev. Relativity **18**, 1 (2015).

[29] Aaron Buikema, Craig Cahillane, G. L. Mansell, C. D. Blair, R. Abbott, C. Adams, R. X. Adhikari, A. Ananyeva, S. Appert, K. Arai et al., Sensitivity and performance of the Advanced LIGO detectors in the third observing run, Phys. Rev. D **102**, 062003 (2020).

[30] Seiji Kawamura and Yanbei Chen, Displacement-noise-free gravitational-wave detection, Phys. Rev. Lett. **93**, 211103 (2004).

[31] Yanbei Chen and Seiji Kawamura, Displacement-and timing-noise-free gravitational-wave detection, Phys. Rev. Lett. **96**, 231102 (2006).

[32] Yanbei Chen, Archana Pai, Kentaro Somiya, Seiji Kawamura, Shuichi Sato, Keiko Kokeyama, Robert L. Ward, Keisuke Goda, and Eugeniy E. Mikhailov, Interferometers for displacement-noise-free gravitational-wave detection, Phys. Rev. Lett. **97**, 151103 (2006).

[33] Atsushi Nishizawa, Seiji Kawamura, and Masa-aki Sakagami, Resonant speed meter for gravitational-wave detection, Phys. Rev. Lett. **101**, 081101(R) (2008).

[34] Keiko Kokeyama, Shuichi Sato, Atsushi Nishizawa, Seiji Kawamura, Yanbei Chen, and Akio Sugamoto, Development of a displacement-and frequency-noise-free interferometer in a 3D configuration for gravitational wave detection, Phys. Rev. Lett. **103**, 171101 (2009).

[35] Yan Wang, Octahedron configuration for a displacement noise-canceling gravitational wave detector in space, in *First-Stage LISA Data Processing and Gravitational Wave Data Analysis* (Springer, New York, 2016), pp. 139–174.

[36] Atsushi Nishizawa, Shoki Iwaguchi, Yanbei Chen, Taigen Morimoto, Tomohiro Ishikawa, Bin Wu, Izumi Watanabe, Yuki Kawasaki, Ryuma Shimizu, Hirohiko Shimizu et al., Neutron displacement noise-free interferometer for gravitational-wave detection, Phys. Rev. D **105**, 124017 (2022).

[37] Glenn De Vine, Brent Ware, Kirk McKenzie, Robert E. Spero, William M. Klipstein, and Daniel A. Shaddock, Experimental demonstration of time-delay interferometry for the laser interferometer space antenna, Phys. Rev. Lett. **104**, 211103 (2010).

[38] Massimo Tinto and Sanjeev V. Dhurandhar, Time-delay interferometry, Living Rev. Relativity **24**, 1 (2020).

[39] D. A. Shaddock, B. Ware, R. E. Spero, and M. Vallisneri, Postprocessed time-delay interferometry for LISA, Phys. Rev. D **70**, 081101(R) (2004).

[40] Junaid Aasi, B. P. Abbott, Richard Abbott, Thomas Abbott, M. R. Abernathy, Kendall Ackley, Carl Adams, Thomas

Adams, Paolo Addesso, R. X. Adhikari *et al.*, Advanced LIGO, Classical Quantum Gravity **32,** 074001 (2015).

[41] Carlton M. Caves and Bonny L. Schumaker, New formalism for two-photon quantum optics. I. Quadrature phases and squeezed states, Phys. Rev. A **31,** 3068 (1985).

[42] Thomas Corbitt, Yanbei Chen, and Nergis Mavalvala, Mathematical framework for simulation of quantum fields in complex interferometers using the two-photon formalism, Phys. Rev. A **72,** 013818 (2005).

[43] See Supplemental Material at http://link.aps.org/supplemental/10.1103/PhysRevLett.132.020801 for further information.

[44] Thomas M. Cover, *Elements of Information Theory* (John Wiley & Sons, New York, 1999).

[45] Jing Liu, Haidong Yuan, Xiao-Ming Lu, and Xiaoguang Wang, Quantum fisher information matrix and multiparameter estimation, J. Phys. A **53,** 023001 (2019).

[46] Petre Stoica and Randolph L. Moses, *Spectral Analysis of Signals* (Pearson, Upper Saddle River, NJ, 2005).

[47] Rosanna Nichols, Pietro Liuzzo-Scorpo, Paul A. Knott, and Gerardo Adesso, Multiparameter Gaussian quantum metrology, Phys. Rev. A **98,** 012114 (2018).

[48] Manuel Gessner, Augusto Smerzi, and Luca Pezzè, Multiparameter squeezing for optimal quantum enhancements in sensor networks, Nat. Commun. **11,** 3817 (2020).

[49] S. P. Vyatchanin and A. B. Matsko, Quantum variational measurements of force and compensation of the nonlinear backaction in an interferometric displacement transducer, Sov. J. Exp. Theor. Phys. **83,** 690 (1996).

[50] Stefan L. Danilishin and Farid Ya Khalili, Quantum measurement theory in gravitational-wave detectors, Living Rev. Relativity **15,** 5 (2012).

[51] Peter R. Saulson, Thermal noise in mechanical experiments, Phys. Rev. D **42,** 2437 (1990).